博士論文要約

論文題目：Study on Improvement of Fresh Properties, Cracking Resistance and Durability of High Flow Concrete Using Industrial By-Products for Eco-Friendly Construction Materials

著者：Benson KIPKEMBOI

1. Preface

The general objective of this study is to promote environmental conservation and sustainability through adoption of eco-friendly construction materials. Since the largest cause of CO_2 emissions in the field of cement industry is the production of ordinary Portland cement (OPC), the reduction of usage of OPC may be a step in the right direction towards environmental sustainability. This study pursues this objective by using high flow concrete which has added advantages over conventional concrete such as improvement of concrete workability, reduction in labor cost, flexibility in design, improved working environment among others. To study the effects of partial replacement of cement (OPC) on high flow concrete, self-compacting concrete (SCC) was used (Ouchi M., Nakamura, S., Osterberg, T. Hallberg, S-E and Lwin, Myint M., 2003). To study high flow concrete using exclusively industrial by-products, alkali activated material (AAM) concrete was used (Provis L. John, & Jannie S.J Van Deventer., 2014).

For SCC, utilization of large amount of binder has been proved to be the greatest contributor to thermal cracking (E. Rozière , S. Granger, Ph. Turcry and A. Loukili, 2007). Previously restraint stress analysis models did not precisely evaluate how much drying shrinkage contributes to cracking in massive concrete that often occur in self-compacting concrete. For SCC, experimental results of concrete properties were used as input parameters to analyze its thermal cracking resistance. Restraint stress due to drying shrinkage was measured on uniaxially restrained concrete specimens and 3D-FEM model was evaluated for accuracy by comparing the results.

Thermal stress analysis was done on 1m thick wall members, and shrinkage cracking resistance of SCC with different replacement ratio of blast furnace slag was discussed. The value of reduction factor for Young's modulus was also proposed to consider the effect of relaxation of drying shrinkage stress caused by creep of concrete. Using the proposed method for the thermal stress analysis, high replacement ratios of blast furnace slag was suggested to improved shrinkage cracking resistance

The challenge with alkali activated material proposed as an alternative to OPC is its poor fresh properties such as low flowability (Yasser Rifaai, Ammar Yahia, Ahmed Mostafa, Salima Aggoun, & El-Hadj Kadri, 2019). There is no clear report investigating particle

packing property as an index to estimate optimum powder combination ratios for improving fresh property. For fresh and hardened properties of AAM paste and mortar with different blend ratio of the powers were tested. Particle packing of blended powder was experimentally and theoretically investigated to discuss its effects on flowability of AAM.

Based on the experimental and analytical investigations, it was concluded that fresh properties and durability of high flow AAM concrete can be improved by optimizing the types, combination and blend ratio of powders from industrial by-products. It can also be concluded that SCC with blast-furnace slag gives a good thermal cracking resistance and that drying shrinkage stress can be precisely analyzed by using the proposed reduction factor for Young's modulus.

It should be noted that the studies on the durability aspect for AAM, which was also one of the important research topics, is not described in the abstract because of the patent application.

2. Experiments

2.1 Materials and mix proportions

Materials mix proportions for SCC used in the study which are majorly industrial by-products such as blast furnace slag, fly ash and silica fumes. The powder (precursor) materials used for AMM were mainly industrial by products materials (IBPM) without any ordinary Portland cement (OPC). These powders were composed of fly-ash (FA), ground granulated blast furnace slag (BFS) with different Blaine fineness (3,290, 4,550, 6530 & 9,510 cm^2/g) – herein designated as BFS3, BFS4, BFS6 & BFS8 respectively, silica fume (SF) and calcium hydroxide (CH) as an activator. In general, BFS4 is the most commonly used powder in Japan. For mortar experiments, ISO standard sand with density ($2.64g/cm^3$), absorption rate (0.42%) and fineness modulus (2.83) was used as fine aggregates. Due to low w/b ratio, Polycarboxylate ether type superplasticizer (SP) commonly used in pre-cast concrete works and de-airing agent (DA) was used. The range of air content of mortar was between 0.7 & 2.9%. The physical properties and chemical composition of powder materials used are shown in Table 2.1 & Table 2.2 respectively.

Paste and mortar experiments for AAM were designed to have a variety of powder blend ratios as shown in Table 2.3. Six blend series were developed based on the BFS: FA blend ratio and in each series, silica fume dosage was varied from 0% to 10%. For reference purposes, experiment using ordinary Portland cement (OPC) – JIS R 5210 (Japan Standards Association, 2021) and conventional blast furnace slag cement in Japan (BB) – JIS R 5211 (Japan Standards Association, 2021) was also carried out. Water to binder (w/b) ratio for all alkali activated materials (AAM) was kept constant at 21%, sand to binder (S/B) ratio at 1.5 & superplasticizer dosage at 1.15% except for series I (1.5%) and the blend with BFS8 which

required 1.8% of SP to achieve reasonable flowability.

Powders need to have certain qualities and characteristic for its application. One such property is particle size distribution. A well graded PSD and spherical morphology of powder are desired to ensure good flowability of powders (C. Gallagher, E. Kerr, & S. McFadden, 2023). Results of PSD show that the powders have a well graded distribution where particles are distributed over a wide range.

Mix proportions of SCC are shown in Table 2.4. Fresh properties of SCC were tested to verify self-compactability equivalent to rank 2 as per JSCE recommendation and concrete specimens were prepared (Japan Society of Civil Engineers, 2012).

Table 2.1: Physical and chemical properties of cementitious materials used for SCC

Cementitious	Density	Fineness		Chemical Composition (%)							
Materials	(g/cm^3)	(cm^2/g)	ig-loss	SiO_2	Al_2O_3	Fe_2O_3	CaO	MgO	SO_3	Na_2O	K_2O
OPC (N)	3.16	3200	0.94	20.84	5.49	3.07	63.89	1.97	2.40	0.40	0.32
BFS	2.90	4590	0.16	32.30	13.93	0.42	42.97	5.68	2.06	0.17	0.29

Table 2.2: Physical properties of the powder materials used for AAM

Powder (Precursor) Material	Powder Symbol	Density (g/cm^3)	Blaine fineness (cm^2/g)	28 days activity index (%)	Reference
Fly-ash	FA	2.20	3,480	81	JIS A 6201
Blast furnace slag	BFS	2.91	4,550	97	JIS A 6206
Silica fume	SF	2.30	191,000	117	JIS A 6207
Silicone Powder	QSG 100	1.80	250,000	-	
Calcium hydroxide	CH	2.32	150,000	-	JIS R 9001

Table 2.3: Mix proportions of concrete for SCC

Mix Name	BFS replacement ratio (%)	W/B (%)	W/P in volume (%)	Abs agg. Vol (m^3/m^3)	Unit Contents (kg/m^3)					AE Cx%	HRWRA Cx%
					Water	Binder (B)		Aggregate			
					W	OPC	BFS	S	C.A		
SCC30	30	33.5	103	0.28	175	366	157	855	739	0.009	0.97
SCC50	50	32.0	97			273	273	828	739	0.012	0.73
SCC70	70	32.5	97			161	376	828	739	0.012	0.66
OPC(N)	0	55.0	174	0.36	180	327	-	812	957	0.001	1.0

Table 2.4: Mix proportions for paste and mortar for AAM

Series	BFS Type	W/B (%)	BFS: FA	Percentage Blend Ratio (%)				Sand	Chem. Admix	Remarks
				BFS	FA	SF	CH	S/B	SP (x B%)	
				0.0	96.0	0.0				
I			0:100	0.0	91.0	5.0		N/A	1.5	Paste only
				0.0	86.0	10.0				
				24.0	72.0	0.0				
II			25:75	22.8	68.3	5.0				
				21.5	64.5	10.0				
				48.0	48.0	0.0				
III	BFS4		50:50	45.5	45.5	5.0				
		21.0		43.0	43.0	10.0	4.0			Paste & mortar
				72.0	24.0	0.0		1.5 – Mortar		
IV			75:25	68.3	22.8	5.0		N/A – Paste	1.15	
				64.5	21.5	10.0				
				96.0	0.0	0.0				
V			100:0	91.0	0.0	5.0				
				86.0	0.0	10.0				
	BFS3			48.0	48.0	0.0				
VI	BFS6		50:50	45.5	45.5	5.0				Mortar only
	BFS8			43.0	43.0	10.0			1.8	

Shapes of the main powder particles used in blending were evaluated by analyzing the images obtained from scanning electron microscope (SEM) as shown in Fig. 2.1 and Fig. 2.2.

It can be seen from the SEM images that the shapes of BFS4 is angular while that of FA is spherical. Due to the effect of interparticle forces, SEM image of SF observed is a conglomerate of many particles while the SEM images of OPC looks crystalline. According to researcher by (Etsuo Sakai, Keisuke Masuda, Yasuo Kakinuma, & Yutaka Aikawa, 2009), the shape of silica fume is spherical. The spherical properties of SF in addition to its high Blane fineness (191,000 cm^2/g), suggest that if it is added to the blend of BFS4 and FA it will further enhance particle packing and flowability.

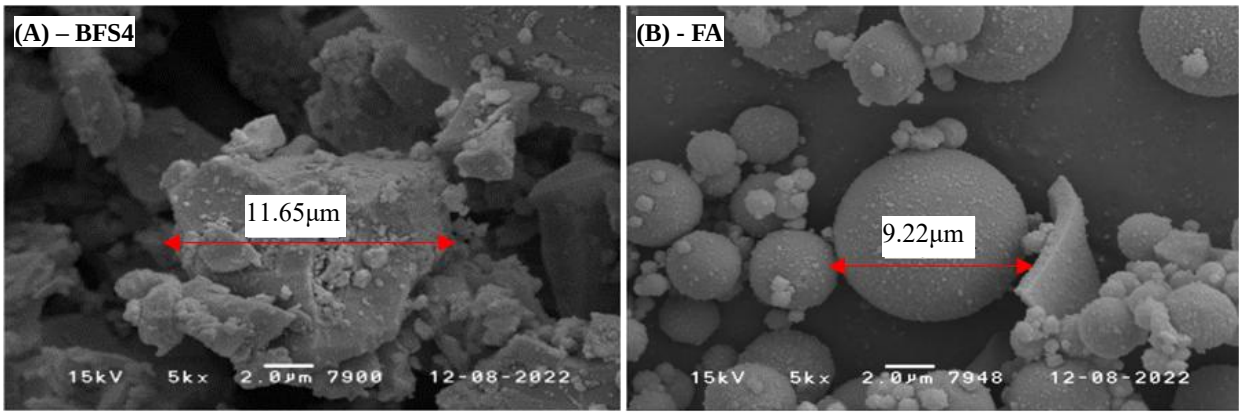

Fig. 2.1: SEM images of BFS4 and fly ash powder

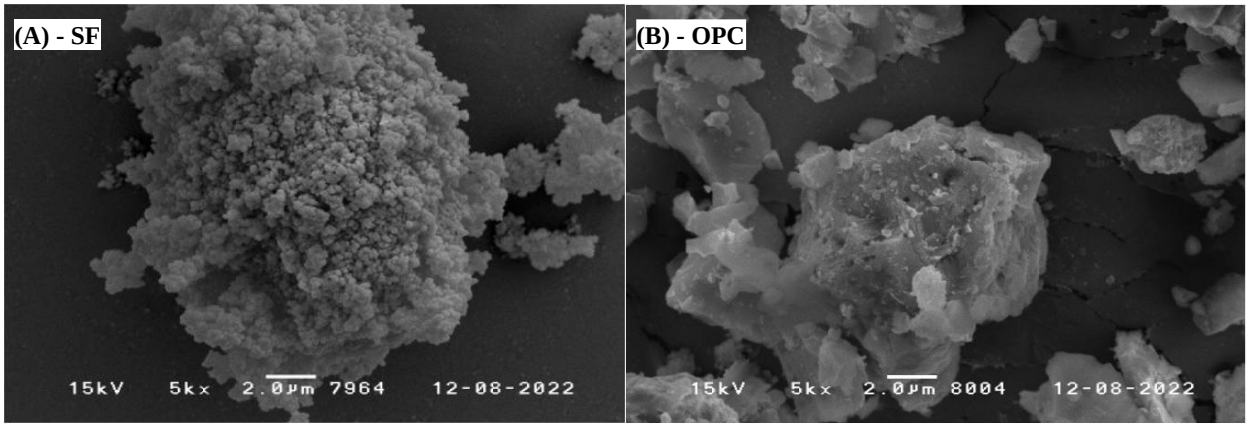

Fig. 2.2: SEM image of silica fume and OPC powder

The results of the particle size distribution (PSD) analyses of the various powder used in the experiment are shown in Fig. 2.3. Distribution parameters / characteristics of each powder are indicated in Table 2.5. Results indicate that the mean and median sizes of the powder particle size used varies.

Table 2.5: Particle size distribution characteristics for the various types of powder used

Particle size distribution	Sample powder							
Characteristics	BFS3	BFS4	BFS6	BFS8	FA	SF (1)	SF (2)	OPC
Mean: - D [4,3] µm	23.612	15.281	11.153	6.051	14.717	12.692	0.344	19.211
D10 µm	2.016	1.886	1.597	1.154	1.695	4.262	0.202	3.021
Median: -D50 µm	14.847	11.627	7.798	4.698	9.195	10.639	0.392	14.834
D60 µm	20.822	15.014	9.790	5.895	12.480	12.530	0.453	18.935
D90 µm	59.150	33.825	25.442	12.834	36.141	23.429	6.555	41.444
Mode µm	25.623	17.226	8.261	6.048	7.959	11.235	0.310	21.581

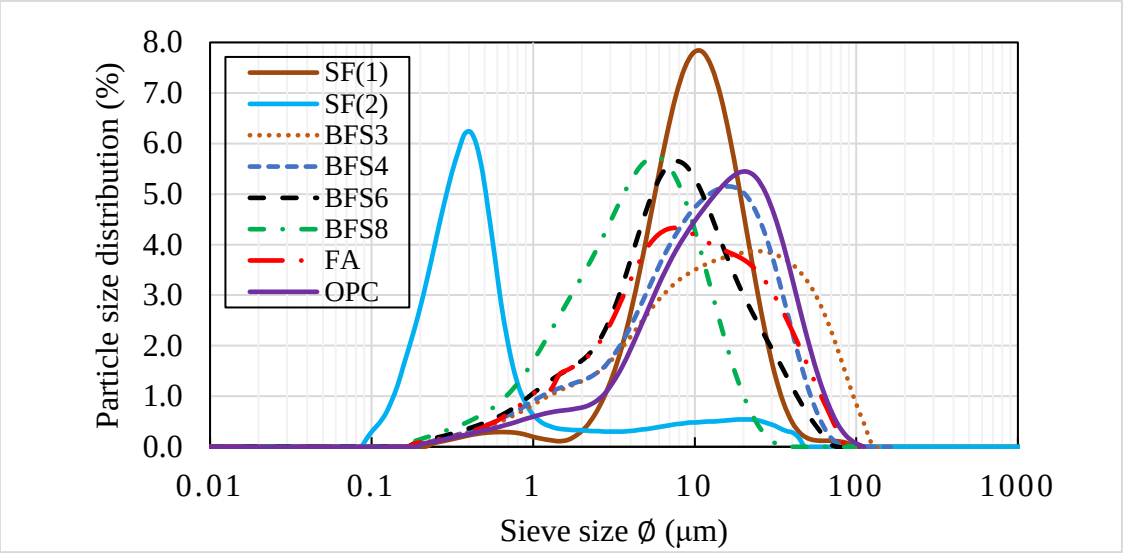

Fig. 2.3: Powder particle size distribution (% mass fraction)

D [4,3] is the mean diameter of particles based on weighted volume, D50 is the median diameter above and below which the particles are the same in volume, D10 and D90 are the diameters below which the proportion of the particles is 10% and 90% in volume, respectively and mode is the modal diameter having the peak of the frequency distribution. The modal diameter represents the particle size range most found in the distribution.

2.2 Experimental procedures

2.2.1 Experiments for SCC

For compressive strength test, specimens were cast on cylindrical molds 100mm in diameter and 200mm depth. The specimens were cured under water at 20 °C and strength test measurements were done at the age of 3, 7, 28 and 91 days according to ASTM C39/C39M-18 (ASTM C 39, 2002). Casting temperature of all the samples was an average of 21 °C with max and min temperature being 24.5 °C and 19 °C respectively.

Temperature rise of concrete due to heat of cement hydration was measured under semi-adiabatic condition. Specimens were cast in insulation molds with internal dimension of 400mm in width, depth and height, which were made of foamed polystyrene with 200 mm in thickness, and the temperature of the central portion of concrete was measured as shown in Fig. 2.3 using embedded strain gauge. The room temperature was kept constant at 20±1 °C throughout the experiment.

Adiabatic temperature rise of the concrete samples was determined using the observed semi-adiabatic temperature rise and it was approximated by Eqn (2.1) (Yasuyuki K., Hirotaka K. and Hiroshi W., 2002).

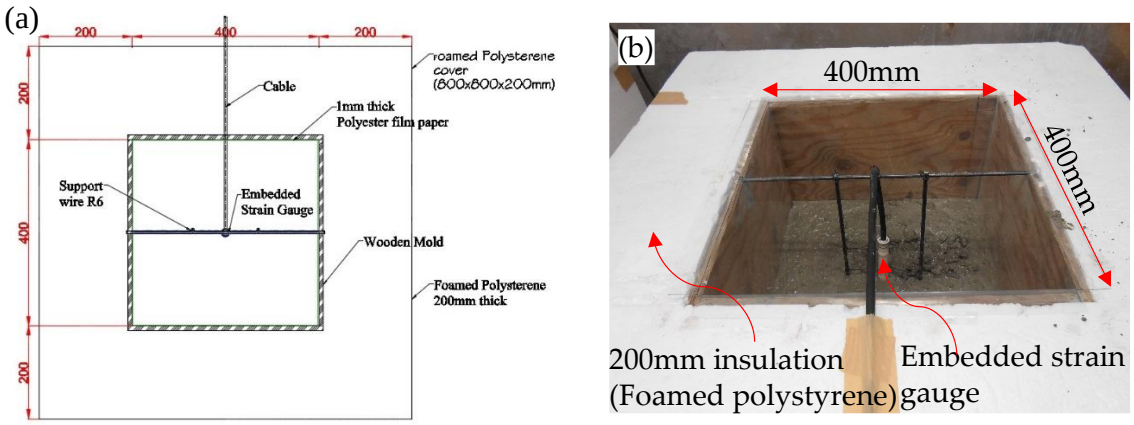

Fig. 2.3: (a) Schematic plan view of the mold and (b) Specimen casting in the mold

$$\rho CVT' - Sh\theta = \rho CV\theta' \tag{2.1}$$

Where,

ρ is the density of the sample specimen (kg/m^3)

C is the specific heat capacity of concrete taken as (1.05KJ/kg^{o}C)

V is the volume of the sample specimen (m^3)

S is the surface area of the sample specimen (m^2)

h is the heat transfer coefficient (W/m^2 ^{o}C) i.e obtained as 0.403 for SCC30, 0.430 for SCC50, 0.485 for SCC70 and 0.450 for OPC.

θ' is rate of change of temperature per second

θ is the adiabatic temperature change with respect to constant room temperature

T is the temperature gradient existing between the sample specimen and the constant room temperature computed as a function of the above-described variables. In the specimens for semi-adiabatic temperature rise tests, the temperature difference between the center and surface of the concrete was very small according to the preliminary experiments.

Adiabatic temperature rise of concrete can also be determined using observed temperature rise under semi-adiabatic condition and is approximated according to Eqn (2.2) of Guidelines for Control of Cracking of Mass Concrete herein referred to as JCI Guidelines (Japan Concrete Institute, 2017). Using a multi-component model for hydration heat, data is fitted by multiple regression analysis and the parameters; Q_∞, r_{AT} and S_{AT} are calculated as functions of cement type, unit content of cement and placement temperature.

$$Q(t) = Q_{\infty}[1 - exp\{-r_{AT}(t - t_{0,Q})^{SAT}\}] \quad (2.2)$$

Where,

t = age (days)

Q (t) = Adiabatic temperature rise (°C)

Q_{∞} = Ultimate adiabatic temperature rise (°C)

r_{AT}, S_{AT} = parameters representing rate of adiabatic temperature rise

$t_{0,Q}$ = age at starting of temperature rise (days)

Autogenous shrinkage strains of SCC specimens was carried out as proposed by Japan Concrete Institute, testing method, chapter 4 (Japan Concrete Institute, 1999). Autogenous strain was measured alongside semi-adiabatic temperature rise at the central portion of the specimen using embedded strain gauge (which can measure strain and temperature rise simultaneously) as shown in Fig. 2.4. Strain measurements was adopted after initial setting time of each mixture. Autogenous shrinkage strain is calculated by subtracting thermal strain from observed strain. Thermal strain is calculated by multiplying temperature change with coefficient of thermal expansion. Coefficient of thermal expansion describes how the size of a material changes with a change in temperature and it varies for each material. For concrete mixtures in this test, coefficient of thermal expansion used was 10 x 10^{-6}/°C. Autogenous shrinkage strain of OPC(N) concrete specimen was predicted using standard equations and constants from JCI Guidelines 2017. This is because OPC is one of the standard types of cements in Japan covered in the JCI guidelines and autogenous shrinkage can be computed precisely without necessarily doing the experiment. This procedure is also described in our previous research (Benson Kipkemboi, Teng Zhao, Shingo Miyazawa, Etsuo Sakai, Nobukazu Nito and Hiroshi Hirao, 2020).

For drying shrinkage test, specimens were cast on molds 100x100x400mm and test carried out according to ASTM C157 (ASTM, 2008). Specimens were demolded after 1 day and cured under water at 20±1℃ until 7 days after casting. Before start of measurement, two contact cells were mounted centrally along the 400mm length face at 300mm apart and the same was done on the opposite face as gauge points. Length change of the specimen was measured between the attached contact cells on each face using a high precision dial gauge. Two specimens were prepared for each mix proportion and stored at 20±1℃ and R.H 60±5%. Drying Shrinkage was measured at 0, 1, 7, 14, 28, 56, 91 and 180 days as shown in Fig. -2. Note that after 1 week, drying shrinkage and autogenous shrinkage is included in the measurement. Since autogenous shrinkage of slender members (in this period) is much less than drying shrinkage, we refer the shrinkage of concrete subjected to drying after 7 days as drying shrinkage.

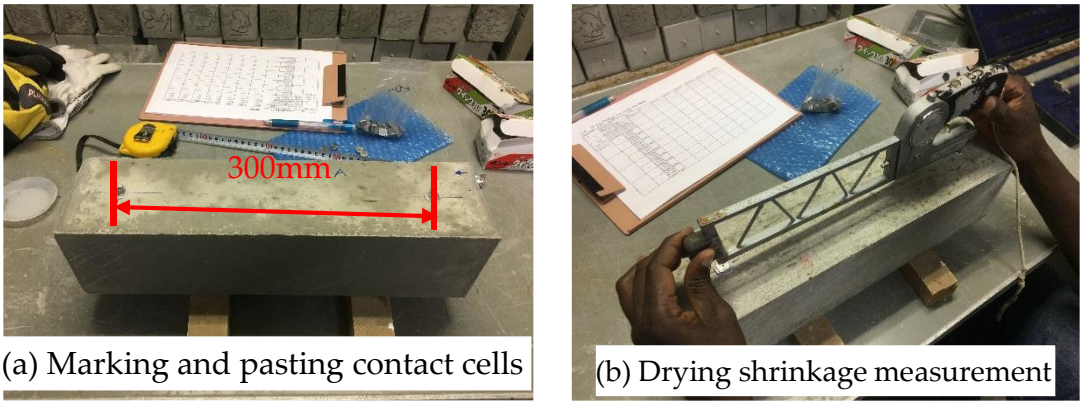

Fig.2.4: Setting and measurement of drying shrinkage strain

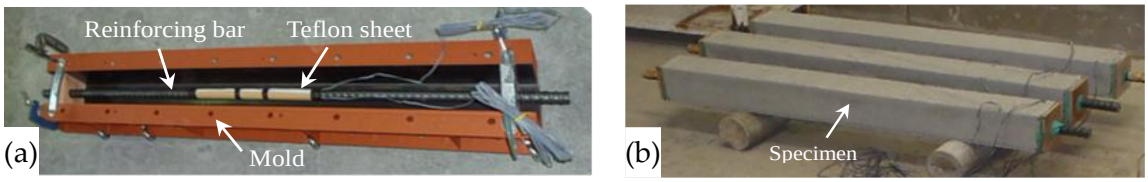

Fig. 2.5: (a) Apparatus for restraint stress test (b) Specimen stored in drying condition

For shrinkage cracking tendency, restraint stress of concrete subjected to drying was measured by uniaxial restraint stress test method. A deformed rebar with nominal diameter of 25mm was embedded at the center of the concrete specimen 100x100x1100mm. Rebar ribs and lugs were removed within the central portion within 300mm.Two strain gauges were attached unidirectional, central and on opposite diametric lines of the portion and sealed with 0.2mm thick Teflon sheet to eliminate bonding between rebar and concrete. After casting concrete, samples were cured under sealed condition for 7 days to simulate actual mass concrete structure other than under-water curing and then exposed to constant drying at 20±1℃ and R.H 60±5%. Measurements of strain on rebar was started and continued until the age of 180 days. Restraint stress of concrete was determined from the strain of the rebar measured by the attached strain gauges. Sudden decrease in strain of the rebar indicate crack on the concrete specimen.

For SCC, experimental results of concrete properties were used as input parameters to analyze its thermal cracking resistance. Restraint stress due to drying shrinkage was measured on uniaxially restrained concrete specimens and 3D-FEM model was evaluated for accuracy by comparing the results.

2.2.2 Experiments for AAM

For fresh and hardened properties of AAM paste and mortar with different blend ratio of the powers were tested. To analyze its rheological properties assuming it as a Bingham body fluid, its flow rate through a J-shaped circular plastic pipe shown in Fig. 2.6 was used. Depth of mortar (hi) under varying pressure and its corresponding flow time (t_i) at every time interval (1 sec) was recorded simultaneously using a laser (KEYENCE LK-G500A) tool kit. Fig. 2.6 shows the J-shaped pipe which was proposed by (Yamamoto Y, Homma A, & Kitsutaka Y, 1996). Corresponding shear stress (P) and shear rate (V) values were computed and relationship graph plotted. As described later, it is proved from the experimental results that the tested mixtures can be assumed to be a Bingham body fluid model thus shear stress (P) and shear rate (V) relationship is given by **Eqn (2.3)**. Shear stress (P) and shear rate (V) values are calculated from the experimental data according to **Eqn (2.4)** and **Eqn (2.5)** respectively.

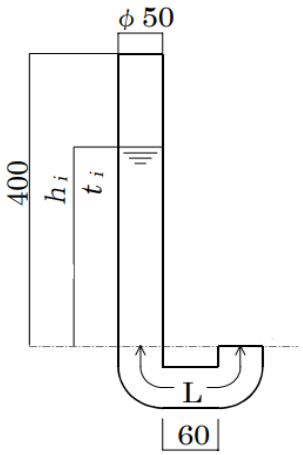

Fig. 2.6: J-Flow experiment set-up (units in mm)

$$P = \lambda \cdot V + \gamma \quad \ldots\ldots\ldots\ldots\ldots\ldots\ldots\ldots\ldots\ldots\ldots\ldots\ldots\ldots\ldots\ldots\ldots\ldots\ldots\ldots\ldots\ldots\ldots\ldots\ldots \text{(2.3)}$$

$$P = \frac{\Delta P \cdot R}{2 \cdot L} = \frac{\rho(h_{i-1}+h_i)}{2} \div C_L + \frac{h_{i-1}+h_i}{2} \cdot \frac{R}{2} \quad \ldots\ldots\ldots\ldots\ldots\ldots\ldots\ldots\ldots\ldots\ldots\ldots\ldots\ldots \text{(2.4)}$$

$$V = \frac{4Q}{\pi R^3} = \frac{4(h_{i-1}+h_i)}{t_i \times R} \quad \ldots\ldots\ldots\ldots\ldots\ldots\ldots\ldots\ldots\ldots\ldots\ldots\ldots\ldots\ldots\ldots\ldots\ldots\ldots\ldots\ldots\ldots\ldots \text{(2.5)}$$

Where,:

ΔP is pressure difference

L is length of the U portion of the J – shaped plastic pipe (24.3cm)

ρ is the density of mortar (g/cm^3)

R is the radius of the plastic pipe (2.5cm)

Q is mortar flow rate / discharge (liters/sec),

C_L is the total length of the J – shaped plastic pipe (400+ L) in cm

h_i is the mortar depth (cm) at time t (sec).

The reciprocal of the resulting trendline slope plotted using Eqn (2.3) gives the mortar viscosity while the horizontal X – axis intercept gives the mortar yield value.

For mortar compressive strength test, specimens were cast in cylindrical molds Ø50mm X 100mm depth according to ASTM C-109-02. To simulate the actual curing condition in the production of precast concrete members, steam curing method was used. After casting, specimens were sealed and placed in the chamber at 20oC for precuring time of 24hr±2hrs. Casting temperature of all the samples was an average of 25 °C. According to research by Kong L. et.al (Kong L., Fan Z., Ma W., Lu J., & Liu Y., 2021), and Maruoka M. et.al (Maruoka M., Fujiwara H., Sugawara T., & Kawato T., 2016) strength development of alkali activated material is very low therefore to avoid interfering with the matrix this experiment adopted 24hrs precuring time before start of steam curing. See Fig. 2.7 for the steam curing temperature profile. The relative humidity of the heating chamber was kept constant at 80%. The specimens were then stored in a room at 20 °C and 60% relative humidity. Compressive strength of the specimens was tested at the age of 14 days.

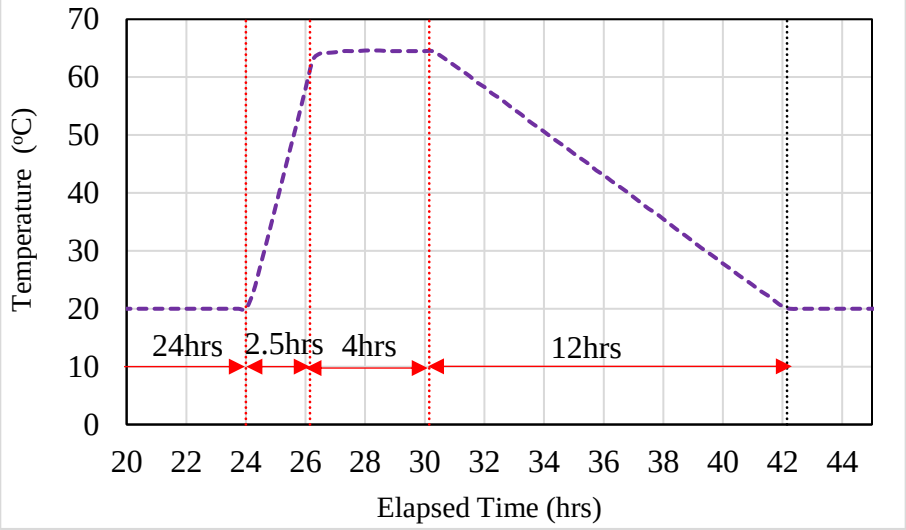

Fig. 2.7: Steam curing temperature profile

3. Results and discussions

3.1 Experimental results and discussions on SCC

Results in Fig. 3.1 show semi-adiabatic and adiabatic temperature rise of concrete specimens. Temperature increase in cast concrete is a result of the heat evolving through the heat of cement hydration. This characteristic property is responsible for thermal cracking in concrete structures at early ages. Rate of adiabatic temperature rise is high in SCC30. This is because in SCC30, the content of OPC in the binder is high. Hydration reaction in OPC is rapid at initial stages due to high C_3S content thus high rate of adiabatic temperature rise. Maximum concrete temperature is high in SCC50 indicating that a lot of hydration heat is generated during hydration reaction. This is due to the high amount of binder used in it. SCC70 concrete specimen have low maximum concrete temperature because of its high replacement ratio of blast furnace slag (BFS). Generally, conventional OPC concrete registered the lowest concrete temperature rise due to high w/c and low binder content used while SCC registered high temperature rise due to low w/c and high amount of powder used. The corresponding constants of heat of cement hydration Q_∞ and r_{AT} of each mix proportion are shown in Table 3.1. These constants are necessary parameters for thermal stress analysis to calculate thermal strain and stress.

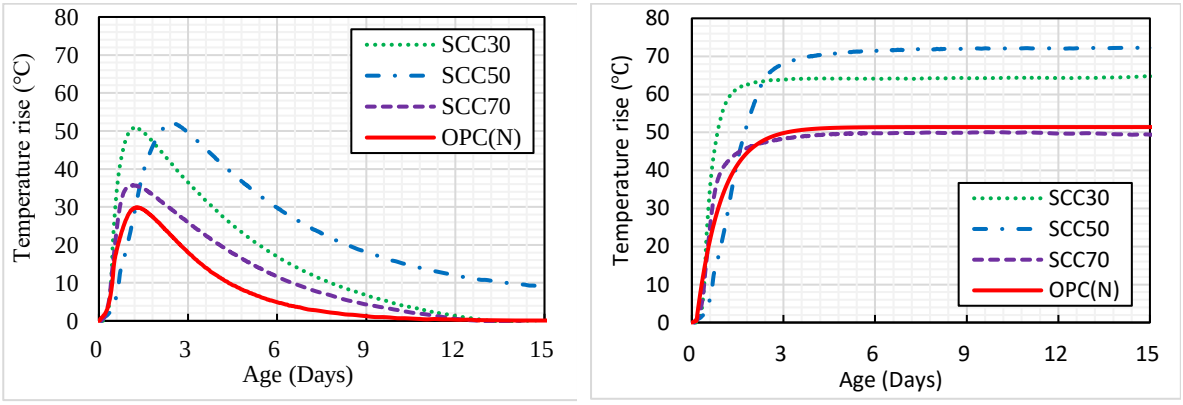

(a) Semi-adiabatic temperature rise

(b) Adiabatic temperature rise

Fig. 3.1: Semi adiabatic and adiabatic temperature rise of concrete specimens

Autogenous shrinkage strain results are shown in Fig. 3.2. Autogenous strain is the self-created bulk strain of cement paste, mortar, or concrete during and after hardening excluding strain due to temperature change. In conventional concrete, autogenous shrinkage strain is not so large, but in concrete with low water-to-cementitious materials ratio (w/c), it is considerably large. Results in Fig. 3.2 agree with this argument in which autogenous shrinkage of SCC concrete samples with low w/c (0.3) has high autogenous shrinkages strain as compared to that of OPC. In their research Yang, Y et.al (Y. Yang, R. Sato and K. Kawai,

2001) suggested that concrete with a low water-to-cement ratio and large amount of binder such as high strength concrete and SCC containing fine granulated blast furnace slag exhibit significant autogenous shrinkage which is due to hydration of the binder. This phenomenon is among the causes of crack generation in this type of concrete.

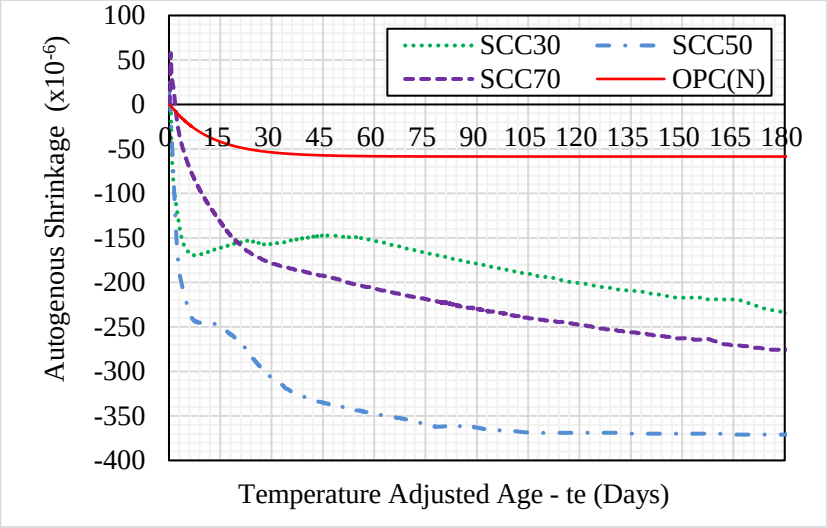

Fig. 3.2: Autogenous shrinkage strain of concrete specimens

According to ACI concrete terminology, drying shrinkage in concrete is the decrease in length or volume change of the hardened concrete due to loss of capillary moisture (American Concrete Institute, 2013). This is a very important property in concrete materials since it also influences its durability. Recent research by Ishikawa et.al (K. Nijs and M. Ishikawa, 2017) indicates that capillary moisture evaporation produces tensile stresses within concrete that leads to concrete cracking. Fig. 3.3 shows the experimental drying shrinkage results of the concrete specimens over a period of six months.

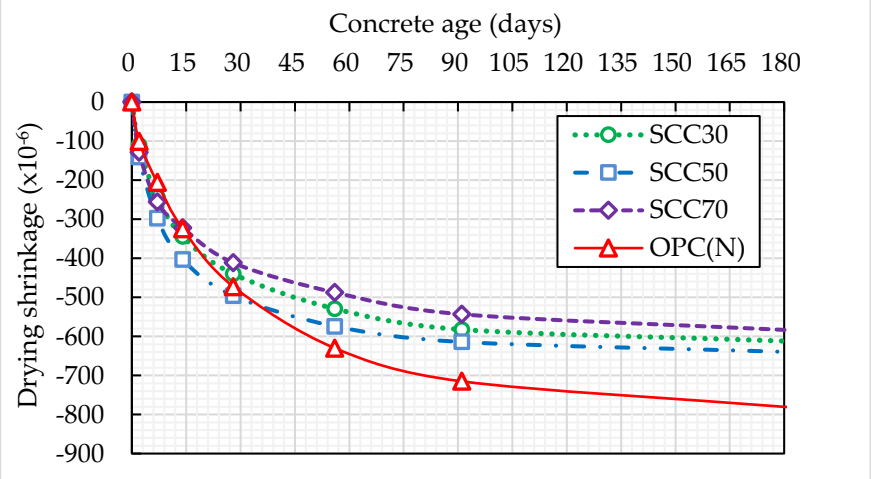

Fig. 3.3: Experimental drying shrinkage strain of concrete specimens

According to ASTM C157 and Japanese Architectural Standard Specification 5 (JASS5), 28-days acceptable drying shrinkage needs to be under 500 and 800 micro-strain respectively for cracking safety. This is on the assumption that after 28 days, concrete has attained enough strength and that influence of drying shrinkage is insignificant. In this experiment, concrete specimens tested meet this 28 day specification requirement with SCC50 experiencing the highest drying shrinkage strain (473μm). Thereafter, after 28 days, as drying continues, drying shrinkage strain keeps increasing. The drying shrinkage trend is maintained by SCC while drying shrinkage rate for OPC becomes higher until the age of 180 days when it's drying shrinkage strain is 782μm. Results also indicates that low water-to-binder ratio in SCC is significant in mitigating drying shrinkage because there is hardly any free pore water available for evaporation. Considering the effects of mineral admixture (BFS) replacement ratio, it can be seen that high replacement ratio i.e. 70% of BFS (SCC70) has low drying shrinkage strain. This result agrees well with the findings of Jamila M.A et.al in which 60% replacement of fly ash reduced long-term drying shrinkage of SCC (J. M.Abdalhmid, A.F. Ashour and T. Sheehan, 2019).

In this study, restraint stress of SCC30, SCC50, SCC70 and OPC(N) concrete samples subjected to drying at 20 ℃ and 60% R.H. was measured. The test results of restraint stress of concrete are shown in Fig. 3.4, in which results of each mixture are expressed as positive values on the vertical (Y) axis. Since the specimens were subjected to drying from the age of 7 days, the restraint stress observed before 7 days is ignored since it is predominantly caused by autogenous shrinkage. This is because free autogenous deformation expand within 1 day and shrinks rapidly from 3 days to 7days and the resultant strains almost cancel out. From the age of 7 days, both autogenous shrinkage and drying shrinkage occur steadily and are the cause of restraint stress with drying shrinkage being the dominant factor for these mixtures. It can be seen from the figure that restraint stresses increased steadily with drying. After an extended drying period, the rate at which stress increases is reduced due to the effect of creep (Wang Guojie, Liu Jiding, Zheng Jianlan and Fan Wei, 2018).

Considering the effect of BFS replacement ratios on restraint stress due to drying, stress build up in SCC30 is higher (2.7N/mm2) than SCC50 and SCC70. This is because of high amount of OPC, which generates a lot heat of cement hydration that causes more stress. High replacement ratio of BFS (SCC50 & SCC70) reduces drying shrinkage stress due to increased presence of calcium silicate (hydration product from BFS) in the mixture, which effectively contributes to reduce porosity and densify the matrix thus mitigating extensive drying (Shasha Xie, Zhiyuan Cheng and Li Wan, 2019). Compared with normal OPC concrete (N), cast without any BFS replacement, it took the shortest time (30 days) before cracks were seen. This indicates that SCC with BFS and low w/b ratio is able to reduce restraint drying shrinkage stress and improve cracking resistance better than normal OPC concrete. The

resistance to shrinkage cracking caused by thermal, autogenous and drying shrinkage of SCC with BFS cement is discussed in the succeeding section.

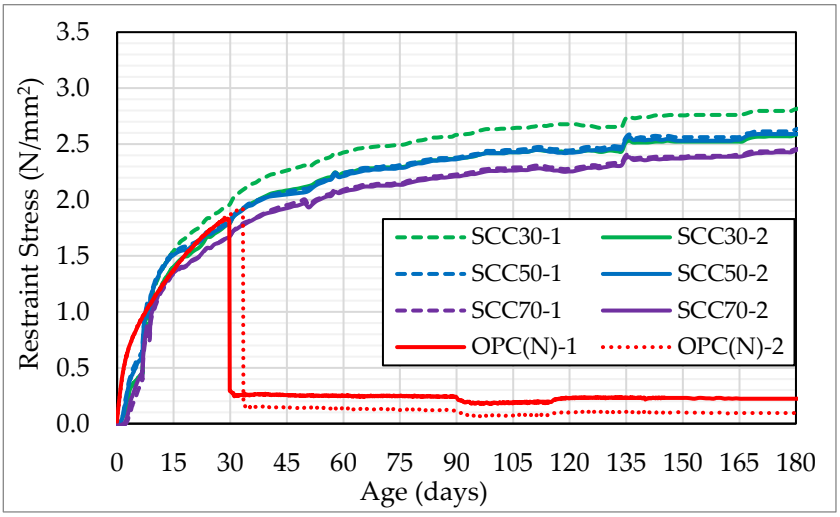

Fig. 3.4: Restraint stress of concrete specimens subjected to drying shrinkage

3.2. Restraint stress analysis for massive SCC subjected to drying shrinkage

Stress analysis of specimen by 3D FEM analysis was carried out using a computer program (JCMAC3) as outlined in Fig. 3.5. Input parameters as obtained from experiment are highlighted in green.

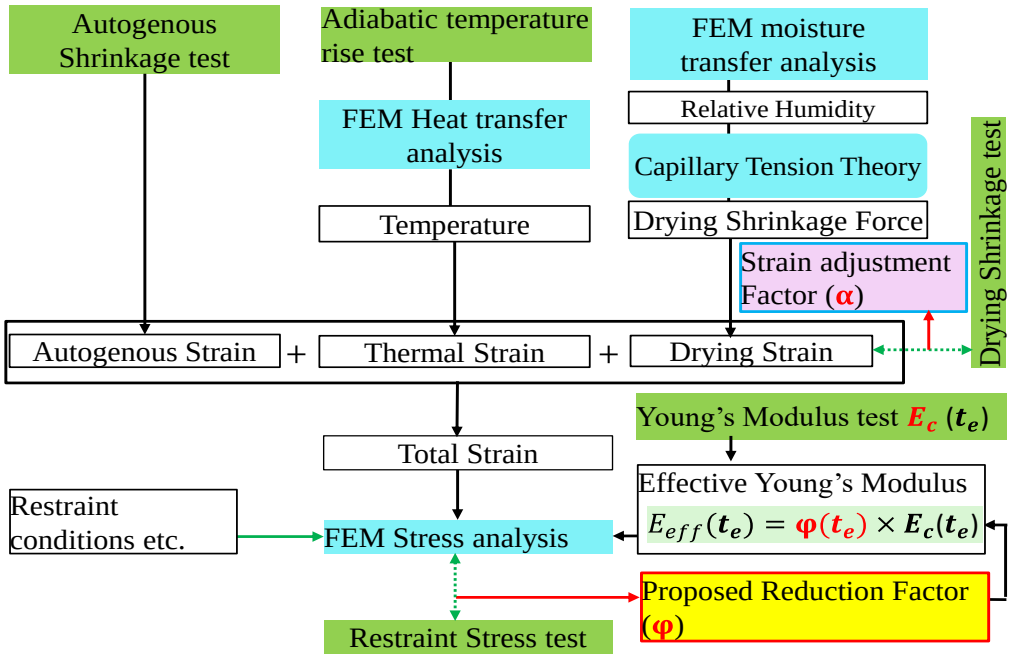

Fig. 3.5: Outline of the flow steps in 3D FEM analysis of strain and stress in concrete

The analysis results is compared with experimental results (restrained stress and drying shrinkage). The influence of creep on concrete stresses is evaluated using effective Young's modulus which is obtained by multiplying Young's modulus by a reduction coefficient $\varphi(t_e)$. Typically, the reduction coefficient used is 0.42 from casting until the age when concrete temperature reaches the maximum and 0.65 at later ages as recommended by JCI guidelines (Japan Concrete Institute, 2008). In this study, a new procedure to consider stress relaxation due to effect of creep in concrete is proposed by modifying the recommended reduction coefficients. The newly proposed reduction factor - $\varphi(t_e)$ was used to precisely evaluate the influence of drying shrinkage on stress of mass concrete structures subjected to long-term drying (180days).

Stress analysis by 3-D FEM program (JCMAC3) was done based on experimental results of concrete properties of each mixture shown in the previous section. In thermal stress analysis, the transient heat transfer was carried out using experimental adiabatic temperature rise of each mixture. Each of the mix proportions has different set of input parameters as summarized in Table 3.1. A constant initial temperature of 20°C was used for all the mixtures.

Table 2.1: Input parameters of concrete properties for use in 3-D FEM analysis

Input parameters	Mix proportions			
	SCC30	SCC50	SCC70	OPC(N)
Thermal properties				
Coefficient of thermal conductivity (W/m°C)	2.7	2.7	2.7	2.7
Specific heat (KJ/kg°C)	1.15	1.15	1.15	1.15
Density of concrete (kg/m^3)	2295	2288	2280	2277
Ultimate adiabatic temperature rise Q_∞ (°C)	64.0	71.2	50.8	51.4
Temperature rise characteristic (r_{AT})	2.16	1.15	1.61	1.22
Effective age at start of heating ($t_{0,Q}$) (days)	0.225	0.100	0.174	0.140
Mechanical properties				
28-day compressive strength (N/mm^2)	63.53	68.54	65.74	34.5
Coefficient (a)	3.204	7.12	3.542	3.686
Coefficient (b)	0.862	0.713	0.876	0.866
Setting time (S_f) - (days)	0.305	0.302	0.214	0.259
Tensile strength coefficient (C_1)	0.13	0.13	0.13	0.13
Tensile strength coefficient (C_2)	0.85	0.85	0.85	0.85
Modulus of elasticity coefficient (C_3)	6300	6300	6300	6300
Modulus of elasticity coefficient (C_4)	0.45	0.45	0.45	0.45
Poisson's ratio	0.2	0.2	0.2	0.2
Autogenous shrinkage	Raw experiment data			

In thermal stress analysis, autogenous shrinkage strain was added to thermal strain and linear elastic analysis carried out whereby stress relaxation due to creep of concrete was considered by using effective Young's modulus (Ec) proposed by Japan concrete institute (Japan Concrete Institute, 2008). . Tensile strength and Young's modulus of concrete in each mixture were determined from the observed compressive strength using Eqn 3.1 and Eqn 3.2 respectively as per the JCI Guidelines. Tensile strength was used to calculate cracking index as an indicator of cracking tendency.

$$f_t(t_e) = C_1 \times f'_c(t_e)^{C2} \tag{3.1}$$

$$E_C(t_e) = C_3 \times f'_c(t_e)^{C4} \tag{3.2}$$

Where; ft (te) is tensile strength of concrete at te (N/mm^2), fc '(te) is compressive strength of concrete at te (N/mm^2), Ec (te) is modulus of elasticity at te (N/mm^2), C_1, C_2, C_3 and C_4 are constants recommended by the JCI guidelines to be 0.13, 0.85, 6300 and 0.45 respectively and te is the temperature adjusted age in days and is computed according to Eqn. 3.3.

$$t_e = \sum_{i=1}^{n} \Delta t_i \times exp\,[13.65 - \frac{4000}{273 + T(\Delta ti)/T_0}] \tag{3.3}$$

Where; Δt_i: Period of constant temperature continuing in concrete (day); T (Δt_i) is concrete temperature for Δt_i (℃) and T0 is 1℃.

Stress relaxation and creep are time dependent variables of concrete. External load or stress applied on specimen may relax gradually due to time dependent properties of concrete (Zhiwei Qu, Ruizhe Si, Pengjiao Jia and Yingda Zhang, 2022). To consider stress relaxation due to creep, a reduction factor - $\varphi(t_e)$ is introduced and multiplied by the Young's modulus of concrete as shown in Eqn 3.4. This reduction coefficient is taken to be 0.42 until the maximum temperature is reached at the adjusted temperature age t_e and 0.65 at later ages from one day after the maximum temperature, $\varphi(t_e)$ is linearly interpolated between 0.42 and 0.65 for the one-day gap.

$$E_{eff}(t_e) = \varphi(t_e) \times E_c(t_e) \tag{3.4}$$

Where:

$E_{eff}(t_e)$ – Effective modulus of elasticity of concrete at t_e

$E_c(t_e)$ – Modulus of elasticity of concrete at t_e

$\varphi(t_e)$ – Reduction factor for modulus of elasticity of concrete.

Drying shrinkage of concrete is affected mostly by properties of the materials used and environmental conditions. It has been shown that the type of coarse aggregates used is also one of the dominating factors affecting concrete drying shrinkage (Hiroshi Yamada, Hiroshi

Katahira and Hiroshi Watanabe, 2018). In order to consider the effect of the variations in each mix proportion on drying shrinkage of concrete, adjustment factor (α) is introduced and used in JCMAC3. During FEM analysis, free drying shrinkage strain of each element is multiplied by the adjustment factor (α) (Kei-Ichi Imamoto, 2008). M. Ishikawa and K. Nijis (K. Nijs and M. Ishikawa, 2017) proposed to use pore size distribution of hardened cement paste to predict free drying shrinkage of typical mixtures in JCMAC3. However, pore size distribution is not a generally obtained information. Therefore, in this study, the standard drying shrinkage test procedure using 100x100x400mm specimen is used to consider the effect of mixture on drying shrinkage instead of pore size distribution.

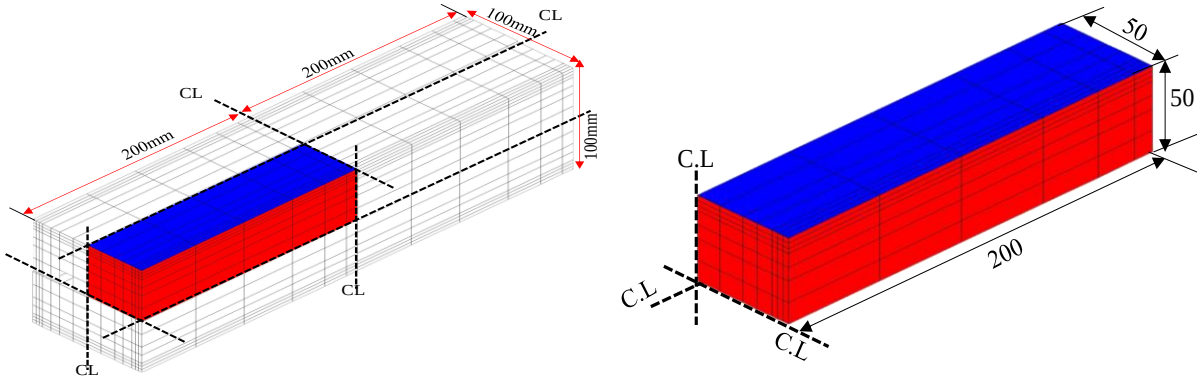

Fig. 3.6: 3D FEM beam model structure for drying shrinkage strain

In order to obtain adjustment factor (α), FEM analyses were done, in which an eighth portion of beam model (50x50x200mm) corresponding to experimental drying shrinkage beam specimen (100x100x400mm) was used as shown in Fig. 3.6. To calculate the drying shrinkage strain in members and structures, the program performs FEM moisture transfer analysis to obtain relative humidity of each element. Then the calculate the radius of evaporated capillary pore water based on pore size distribution and drying shrinkage force in the remaining capillary pore water is computed. Based on capillary tension theory free drying shrinkage strain of each element is computed. Using pore parameters of each mix proportion and capillary tension theory, drying shrinkage force is computed. This concept is based on the general fact that when the water existing inside the pore evaporates, tensile force is exerted which acts by pulling the walls of the pores towards each other. In this analysis, typical pore size distribution for normal concrete with water-to-cement ratio of 45% reported by M. Ishikawa was used (K. Nijs and M. Ishikawa, 2017).

Drying shrinkage strain of the specimen from FEM analysis is then compared with experimental drying shrinkage and appropriate strain adjustment factor (α) is computed. This factor is unique to each mix proportion. Thermal strain and autogenous strains are also computed using heat of cement hydration and autogenous shrinkage data of each mix

proportion respectively. These strains are much less than drying shrinkage strain in the specimens with such a small dimension and under drying condition (Maruyama Ippei, 2022).

Results of 3 D FEM analysis for drying shrinkage strain of the specimens are shown in Fig. 3.7 to Fig. 3.10. In this study, strain adjustment factor (α) was determined so that drying shrinkage of the specimen from FEM analysis fits the experimental value after 180 days of drying. However, the rate of drying shrinkage from FEM results is larger than that from the experiment. The difference is attributed to by the fact that the similar pore size distribution was used for each mixture in FEM analysis. In the future, for more precise calculation, it is recommended to measure and use pore size distribution of each mixtures.

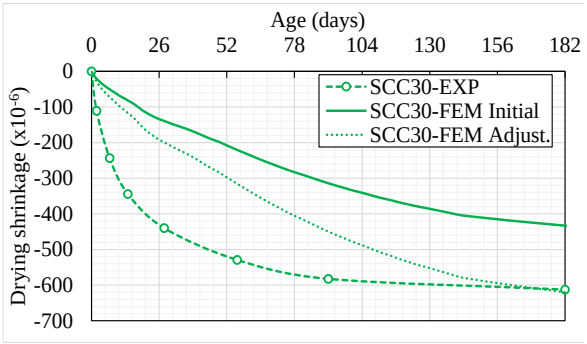

Fig. 3.71: Adjustment of SCC30 FEM strains

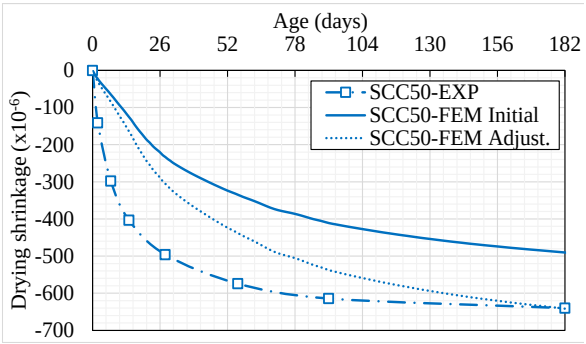

Fig. 3.82: Adjustment of SCC50 FEM strains

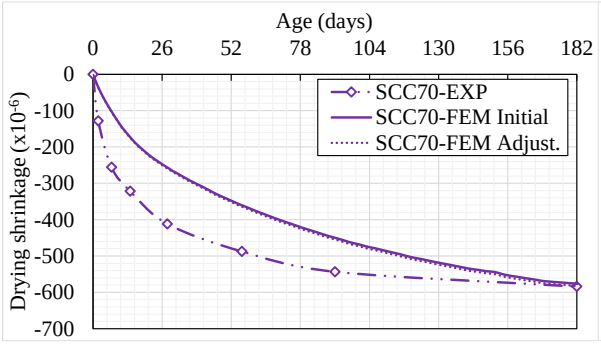

Fig.3.9: Adjustment of SCC70 FEM strains

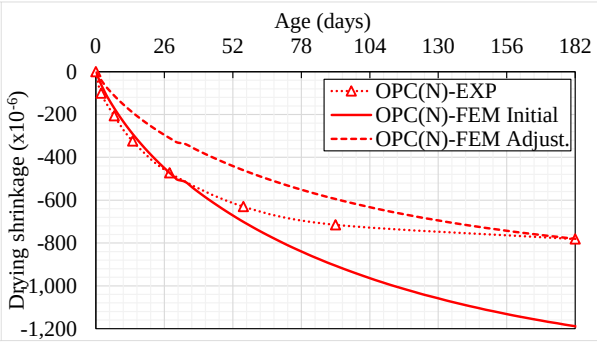

Fig.3.10: Adjustment of OPC(N) FEM strains

The adjustment factors for each mix proportions are shown in Table 3.1. These factors will be utilized in restrain stress analysis described later. The trend in FEM analysis strain is similar with the trend in experimental strains. SCC exhibits low drying shrinkage strain compared with OPC concrete.

Table 3.1: Strain adjustment factors (α) in FEM analysis for drying shrinkage

Mix proportion	SCC30	SCC50	SCC70	OPC(N)
Adjustment factor	**1.43**	**1.31**	**1.01**	**0.65**

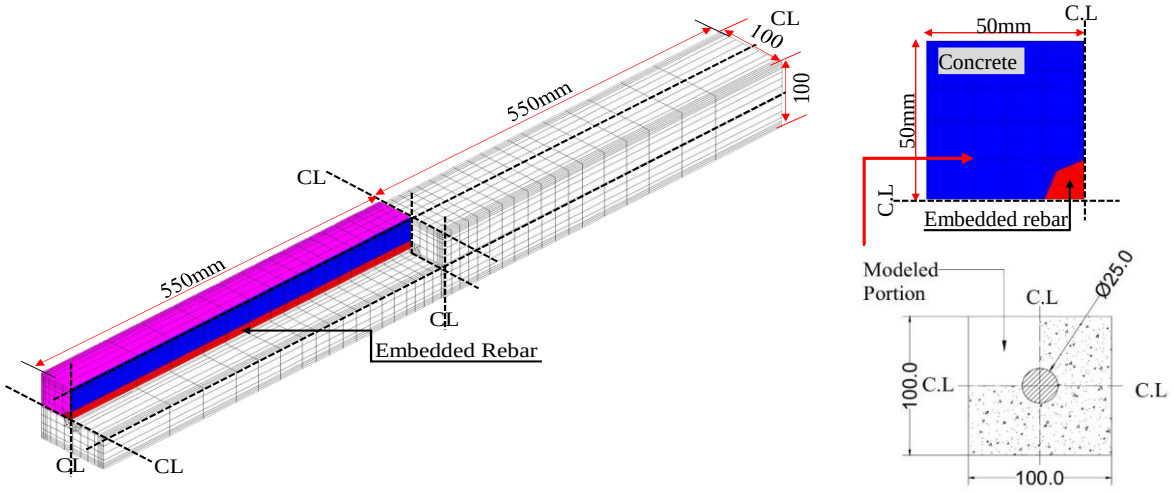

Fig. 3.113: 3D FEM beam model structure for restraint stresses due to drying shrinkage

For 3D FEM analysis of restraint stresses due to drying shrinkage, An eighth portion of beam model (50x50x550mm) corresponding to experimental restraint stress due drying shrinkage beam specimen (100x100x1100mm) was used as shown in Fig. 3.11. Corresponding experimental data of each mix proportion as autogenous shrinkage, adiabatic temperature rise, drying shrinkage and material properties necessary for analysis is input. In addition, adjustment factor obtained from strain adjustment is included as input data. Restraint stresses due to drying for each mix proportion is analyzed. 3D FEM analysis stresses and experimental restraint stress due to drying of each mix proportion were compared and an appropriate reduction factor - $\varphi(t_e)$ for effective young's modulus of elasticity was proposed. This is a factor that can give output stress almost same as the experiment stress. This factor is independent of the individual mix proportions.

Note that to calculate restraint stresses due to temperature change and autogenous shrinkage (Ignoring drying shrinkage), conventional reduction factor $\varphi(t_e)$ is used in the program to compute effective Young's modulus of elasticity - $E_{eff}(t_e)$. The dotted line shown in Fig.3.12 is the conventional reduction factor $\varphi(t_e)$. This conventional value $\varphi(t_e)$ is normally sufficient for stress analysis in concrete within a short period of a few weeks after casting to about 2 months. In their research, Ryoichi A. et.al considered reduction factor - $\varphi(t_e)$ of young's modulus of early age concrete younger than 2 weeks and found that reduction factor varies with varying hydration temperature of the concrete specimen (Ryoichi A., Mizobuchi T. and Izumi H., 2019). When the conventional reduction factor $\varphi(t_e)$ is used, the stresses increase gradually almost infinitely contrary to the experimental results.

In this study, a new procedure to consider stress relaxation due to effect of creep in concrete is proposed by modifying the value of conventional reduction factor (t_e) as shown in Fig. 3.12.

The proposed value of $\varphi(t_e)$ was assumed to be constant for each mixture as is the case for the conventional value of $\varphi(t_e)$, and was determined so that the analyzed stress approximately agree to those obtained by the experiments.

Analysis and experimental results are compared and shown in Fig. 3.13 to Fig. 3.16. It can be seen that the calculated stress using the proposed value of $\varphi(t_e)$ has better results than using the conventional value of $\varphi(t_e)$. It is noted that the value of $\varphi(t_e)$ is taken to be a relatively small value as shown in Fig. 15. Since drying shrinkage increases very slowly for an extended period, effective Young's modulus should be considerably small value in elastic analysis to consider large effect of creep of concrete. From the results, It can be said that the new proposed reduction coefficient precisely evaluate restraint stress of SCC subjected to long term drying.

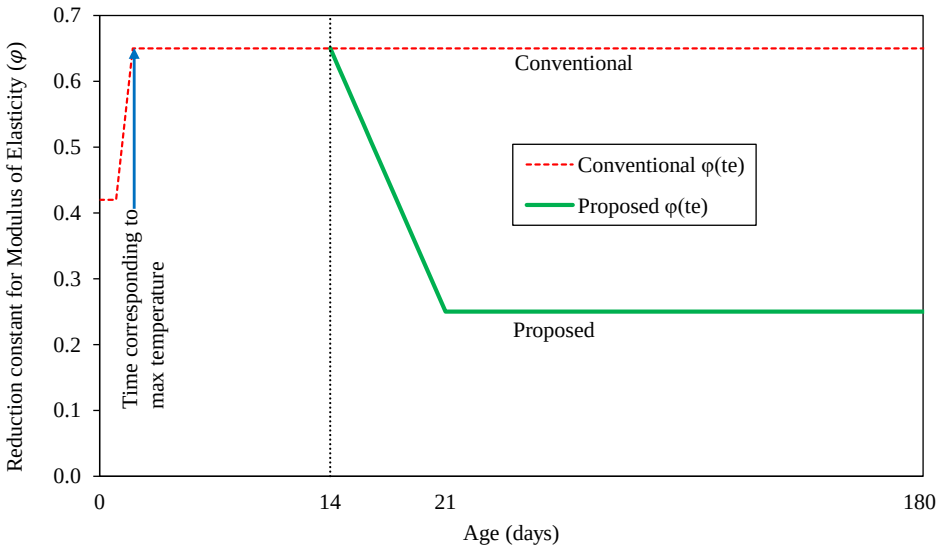

Fig. 3.124: Proposed reduction coefficient for modulus of elasticity of concrete

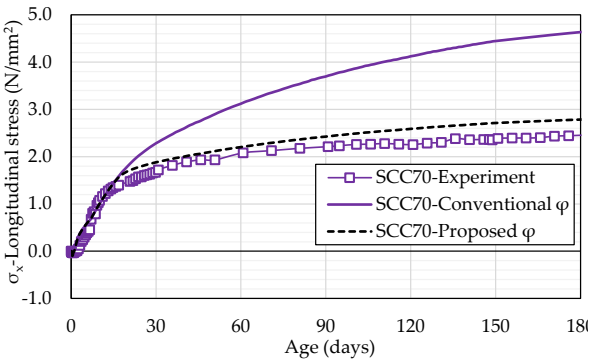

Fig. 3.13: Restraint stress in SCC70

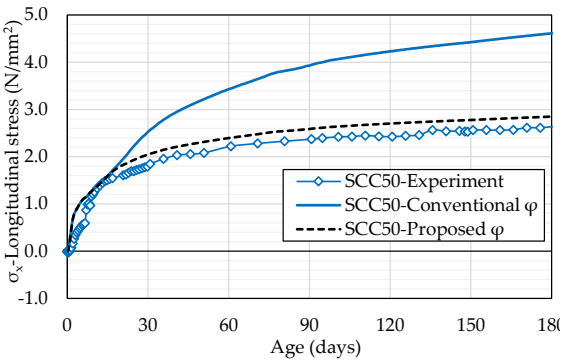

Fig. 3.14: Restraint stress in SCC50

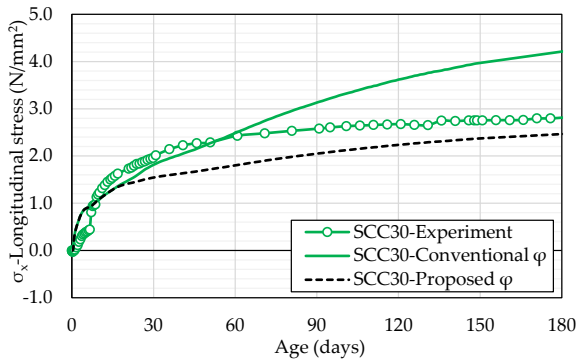

Fig. 3.15: Restraint stress in SCC30

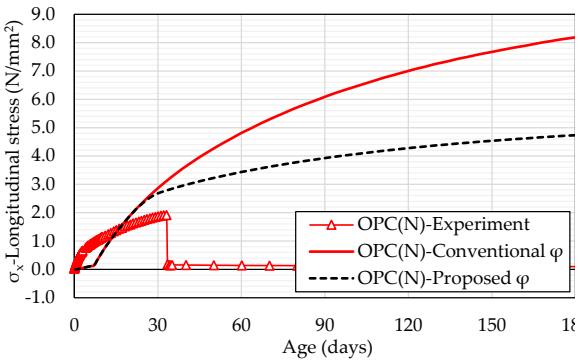

Fig. 3.16: Restraint stress in OPC(N)

3.3 Estimation of cracking resistance of SCC mass structure considering drying shrinkage

To discuss cracking resistance of SCC in actual mass concrete structure applications, FEM analyses were carried out to simulate the restraint stress due to temperature change, autogenous shrinkage and drying shrinkage generated in wall-type model structure as shown in Fig. 3.17.

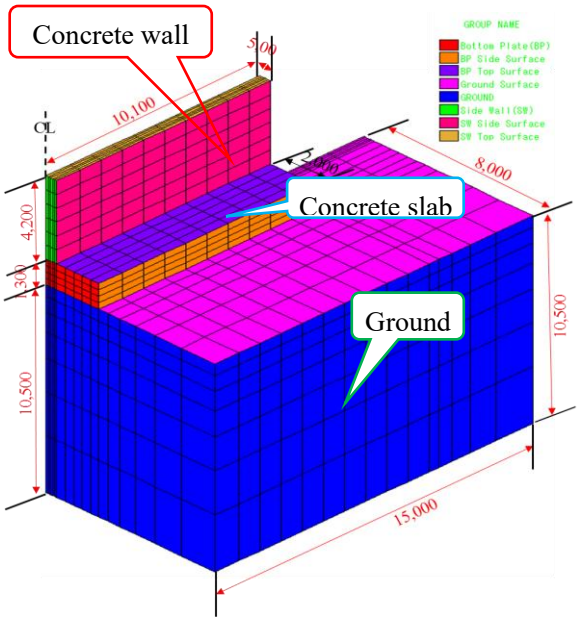

Fig.3.17: Model structure of actual wall mass concrete for use in 3-D FEM

The thickness of the wall is 1.0m, height is 4.2m and length is 20.2m. In FEM analysis, one-fourth model is used. Wall concrete is cast one month after slab concrete was cast and the wall is subject to drying in the atmospheric conditions at 20℃ and 60 % relative humidity after formwork removal at the age of 7 days. The coefficient of heat transfer of the mold is assumed to be 14W/m^2°C. The experimental concrete properties of each mixture shown in Table 3 were used. The proposed reduction factor - $\varphi(t_e)$, which is shown in Fig. 15 was used to evaluate the influence of drying shrinkage for extended period (180 days). Analysis results indicate that tensile restraint stress in the longitudinal direction generated in the wall member is dominant. The stresses are discussed as the main cause for cracking in this type of structure.

In order to evaluate cracking tendency of mass concrete structures, cracking index is used. Cracking index is defined as the ratio of tensile strength of concrete to tensile stresses as shown in Eqn 3.5, which is proposed by the JCI Guidelines for control of cracking of mass concrete.

$$I_{cr} = \frac{f_t(t_e)}{\sigma(te)_{max}} \quad (3.5)$$

Where,

I_{cr}: Cracking index

$f_t(t_e)$: tensile strength (N/mm^2)

$\sigma(t_e)max$: maximum principal stress (N/mm^2)

t_e: temperature-adjusted age (day)

For crack control in mass concrete structures, restraint stress caused by temperature change due to cement hydration and autogenous shrinkage is generally analyzed for the period from 1 to 2 months. This period is dependent on the thickness of the member and about 1 month is recommended by JCI Guidelines for the current model structure (Japan Concrete Institute, 2008). Results from 3D FEM analysis show that at about 1 month, the critical region with low cracking resistance is at the center (core) of the structure as shown in Fig. 3.18 and agrees well with the trend in our previous research (B. Kipkemboi and S. Miyazawa, 2018). This trend is due to influence by large heat of cement hydration and autogenous shrinkage, which produces dominant cracking, stresses. Temperature rise due to cement hydration is higher in the core than the surface of the wall. This results in larger thermal shrinkage corresponding to the large temperature decrease. This non-uniform strain in the cross section leads to tensile stresses at the core, which is caused by internal restraint.

At the core of the structure, the stresses are higher as shown in Fig 3.19. Generally, SCC develop high stresses as compared with OPC. The trend of stress generated corresponds to that of heat of cement hydration. This is due to the high heat of cement hydration caused by high amount of binder content and low water-to-binder (w/c) ratio.

Cracking index analysis of the wall structure at the core indicates that the three mix proportions of SCC have low cracking index than the control specimen (OPC) as shown in Fig. 3.20 This shows that SCC has a low cracking resistance at an early age compared to OPC. SCC70 has the highest cracking resistance. This is because of the high replacement ratio of blast furnace slag. SCC50 has the lowest cracking index indicating a low cracking resistance. This is because of the high restraint stresses occasioned by high autogenous shrinkage. After a short period of about 10 days, the cracking index in all mixtures drops significantly before becoming constant. The significant drop is associated with the temperature changes that occur when concrete temperatures decrease. The core is not affected by the drying condition, which occurs at the surface of the member since thick layer of concrete acts as an insulation.

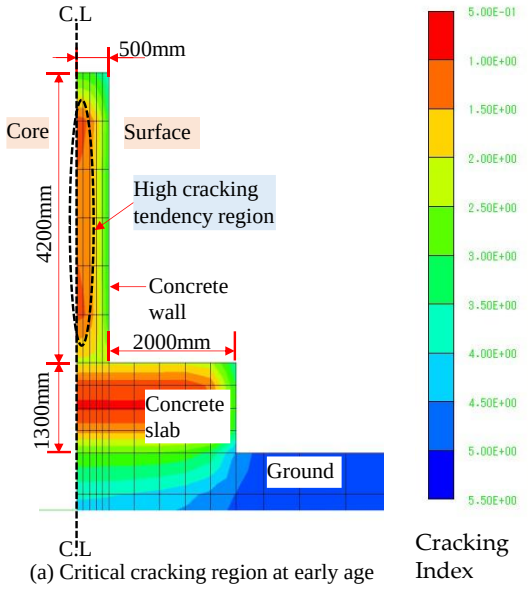

(a) Critical cracking region at early age

Fig. 3.18: High cracking tendency region of the concrete wall structure at early age

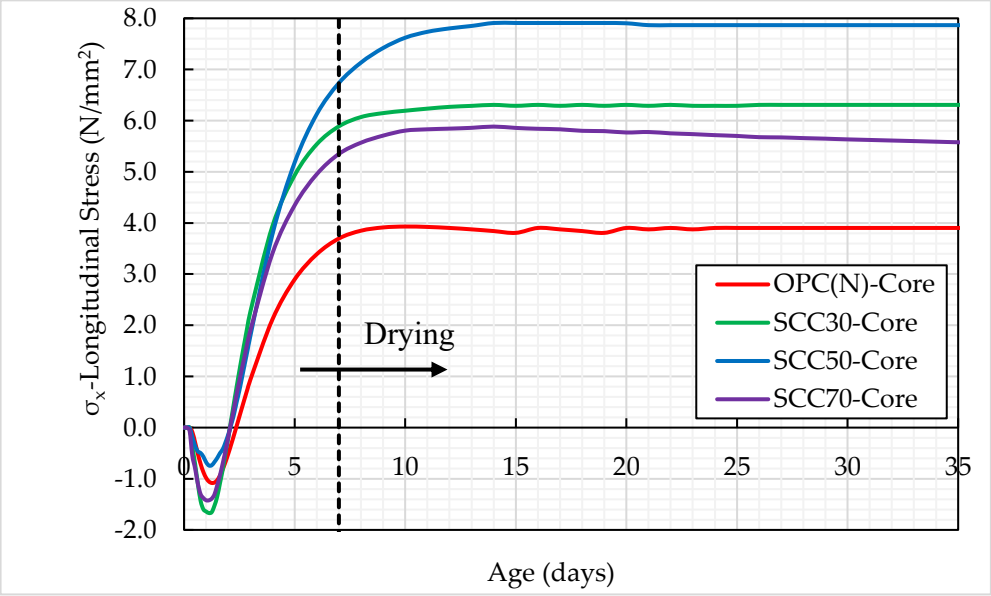

Fig. 3.19: Stresses at the core of the concrete wall structure at early age

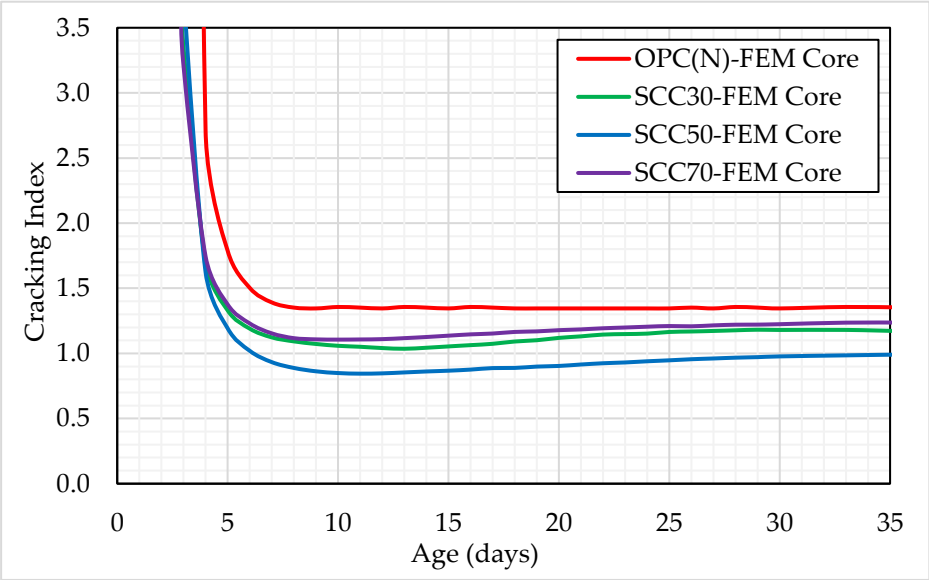

Fig. 3.20: Cracking index of the concrete wall structure at early age

When concrete is subjected to drying for an extended period, drying shrinkage stresses is superimposed on thermal stresses and autogenous shrinkage stress. In this case, the critical cracking tendency region shifts from the core of the surface of the structure as shown in Fig. 3.21. Drying shrinkage becomes the predominating factor and critical cracking region occur at the surface of the member.

Stress analysis results of the mass concrete structure exposed to drying for an extended period of time is shown in Fig. 22 for the core and surface. Results show that SCC50 experiences the highest stresses. This is because of the high heat of hydration and autogenous shrinkage associated with it. At the core, OPC has low stresses. This is due to low temperature rise and low autogenous shrinkage. When the structure is subjected to drying for an extended period up to 6 months, the trend at which stress is developed in the surface changes. Stress increases gradually as time increases. In the case of SCC, SCC50 has the highest stresses. SCC70 however becomes the second most critical while SCC30 develops low stresses. SCC30 has the lowest stress and this is largely due to its low autogenous shrinkage explained earlier.

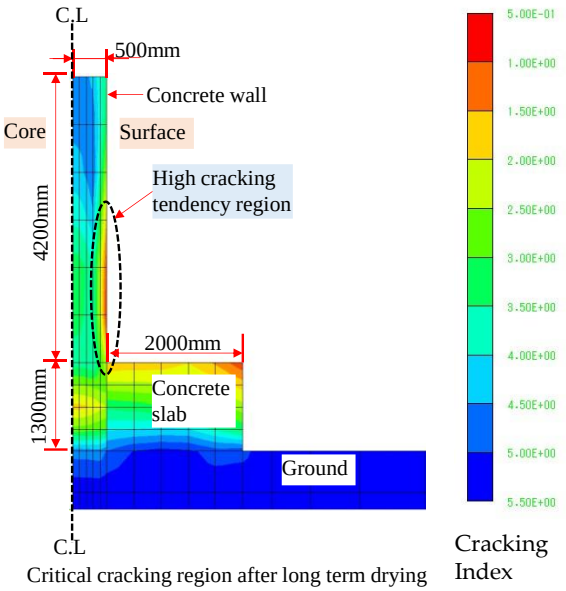

Fig. 3.21: Critical cracking region of the concrete wall at extended drying age

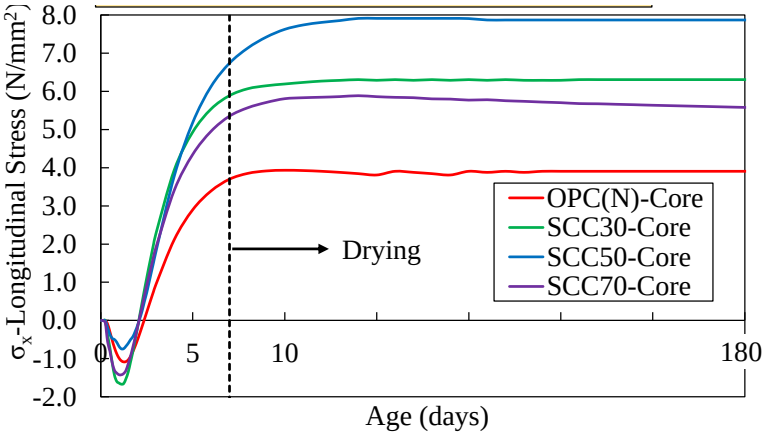

(a) Stress at the conrete core at extended drying ages

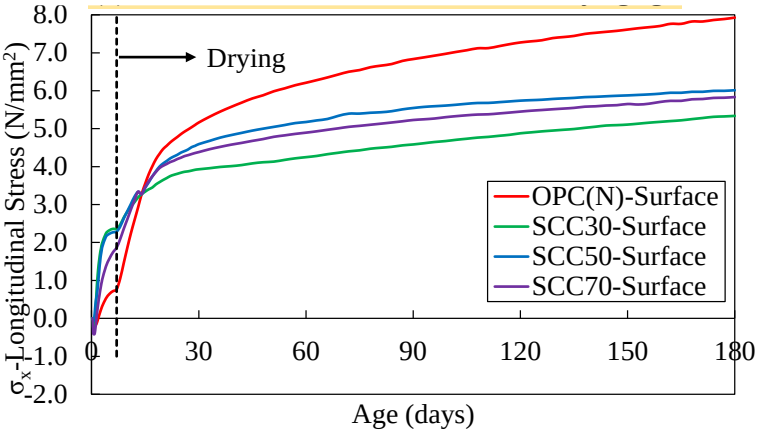

(a) Stress at concrete surface at extended drying ages

Fig.3.22: Stresses at the core and surface of the concrete subjected to drying

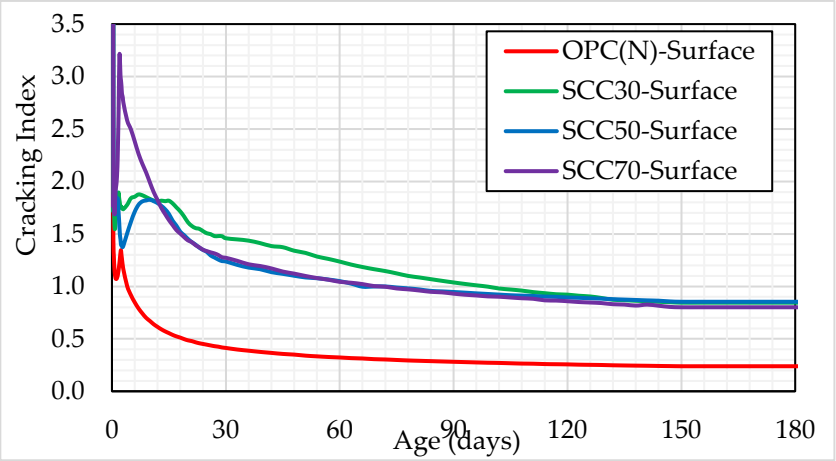

Fig. 3.23: Cracking index at the surface of the concrete wall subjected to drying

At an extended age, critical regions with low cracking resistance is at the surface of the wall. Analysis results of concrete cracking index at the surface of the wall at an extended age when subjected to drying are shown in Fig. 3.23

When subjected to extended period of drying, the surface of the concrete becomes critical. Considering cracking index at the surface of the structure, the trend is different from that at the core. At an extended drying age, SCC50 has high cracking index indicating that at as drying continues, it becomes better in cracking resistance than SCC30 and SCC70. This is because SCC50 has a high 28 day compressive than SCC30. This influences the calculation of splitting tensile strength, which is used to calculate cracking index. This shows that cracking resistance of each mix proportion may also depend on the exposure condition of the structure and its strength at control age (28 days). Research by Amir Hossein and Mahmoud Nili also showed that, SCC is better than OPC concrete in crack resistance when subjected to extended drying condition (Amir Hossein Ghorbankhani and Mahmoud Nili, 2021).

4. Results and discussions on AAM

4.1 Estimation of cracking resistance of SCC mass structure considering drying shrinkage

From the experimental results shown in Fig. 4.1, the relationship between shear stress and shear rate for all the mix proportions is almost a straight line within the range of shear stress applied in the experiments. This implies that the flowability of mortar mixtures can be analyzed as a Bingham body fluid or Newtonian fluid depending on whether the flow curve has a yield value or not. Therefore, viscosity and yield values can be computed. Variations in the slope of the trendline indicates variations in the flow properties viscosity according to each mix proportions.

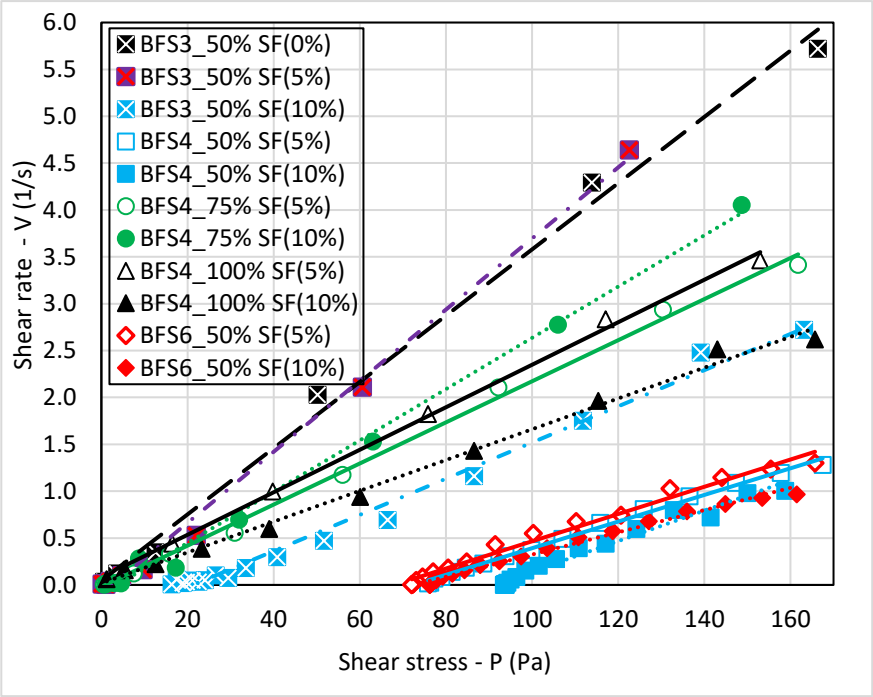

Fig. 4.1: Relationship between shear rate and shear stress of mortar mix proportions

Mortar flow value results from flow table flow tests are shown in Fig. 4.2 indicate that for each ratio of BFS:FA, better flowability is achieved at 5% SF dosage as compared to the other SF dosage. This can be explained by the effect of good particle packing which reduces the void fraction of the blend powder making available the amount of free water necessary to improve flowability. It was observed that mortar mix proportion with BFS: FA of 75:25 and 100:0 exhibited a flow phenomenon where the surface forms viscous (hard skin like) cover at the time of shoveling yet they could flow considerably with time. A similar phenomenon was also observed in AAM and described by (Maruoka M., Fujiwara H., Sugawara T., & Kawato T., 2016) as dilatancy. In order to discuss quantitatively the dilatancy behavior of this kind of material, further experiments with applied pressure level should be done in the future.

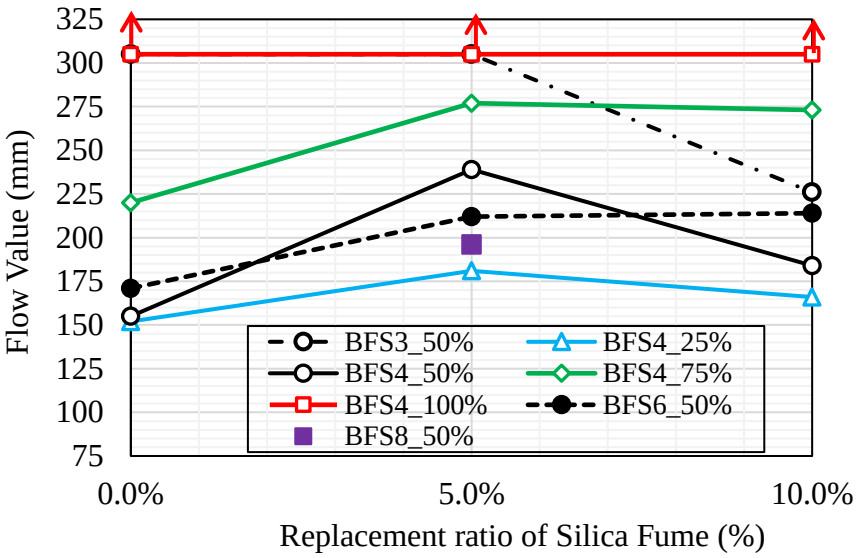

Fig. 4.2: Effects of % dosage of silica fume on mortar flow value

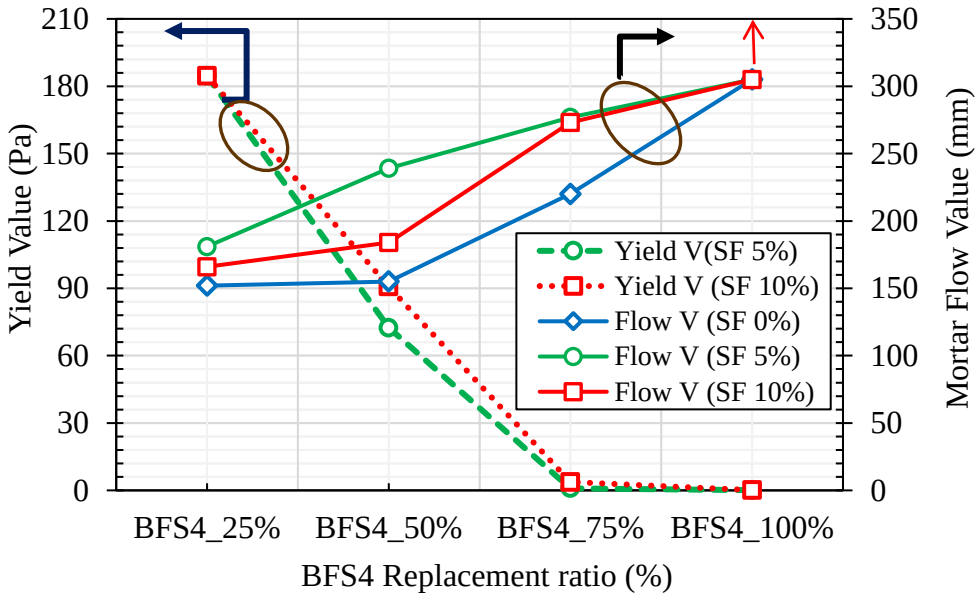

Fig. 4.3: Effects of BFS4 replacement ratio on flow and yield values of mortar

Fig. 4.3 indicates that increasing the ratio of BFS4 drastically reduces the yield value while flow value increases making mortar highly flowable. It has been reported by various researchers (Juntao Ma, Daguang Wang, Shunbo Zhao, Ping Duan, & Shangtong Yang , 2021) that particles which are rounded (spherical) in shape can increase fluidity / flowability

of the composite mix. These results suggest that the addition of fly-ash to the mixture reduces the surface friction of blended powder due to its spherical (ball bearing effect) shape thus supplementing each other to increase fluidity. However, due to dilatancy conditions associated with proportion BFS: FA of 75:25 and 100:0, its flowability is also compromised. This condition may cause problems in actual execution. This leaves proportion with BFS: FA of 50:50 and SF dosage of 5% as the best combination with good flow properties.

In their previous research (Kong L., Fan Z., Ma W., Lu J., & Liu Y., 2021), reported that under standard curing at a constant temperature of 20°C the strength of AAM mortar with fly ash (FB) was low - 1.3 N/mm² - at 3 days and improved significantly to 25 N/mm² at 1 day when steam curing was used at a max temperature of 80°C. In this research steam curing according to the temperature profile shown in Fig. 2.7 was adopted and compressive strength test of specimens was tested at the age of 14 days.

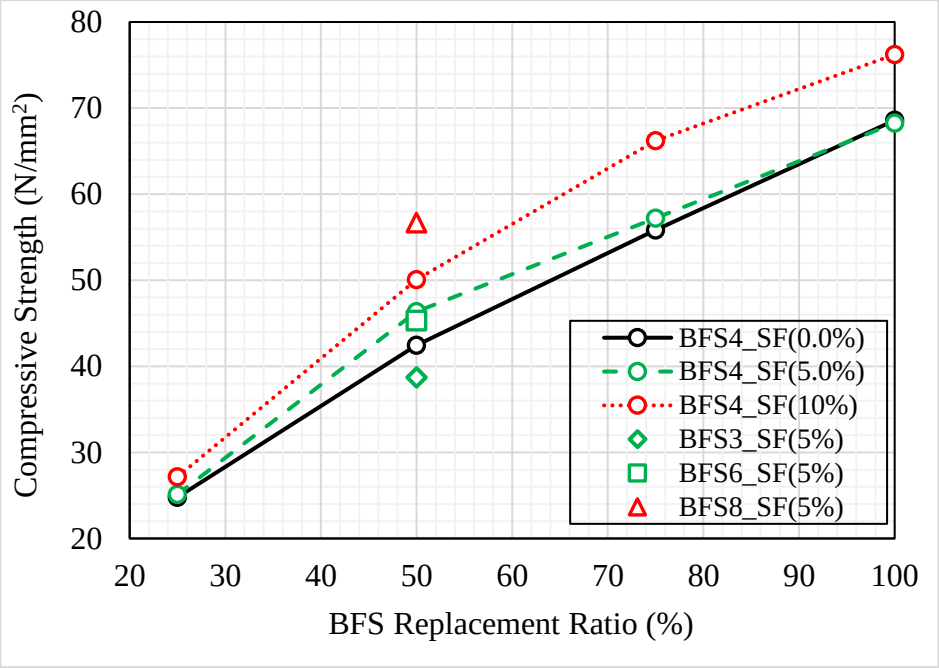

Fig. 4.4: Compressive strength of steam cured mortar at 14 days.

Compressive strength results of mortar specimens are shown in Fig. 4.4. It indicates that increasing the proportion of BFS4 and the dosage of silica fume (SF) increases compressive strength of the alkali-activated materials. This is due to increased availability of high calcium supplied from BFS4 which plays an important role in C-H-S hydration reaction (Zhijie Yang, et al., 2022). Generally speaking with regards to strength only, the best combination would be BFS4: FA 100:0 with 10% dosage of SF. However, due to high dilatancy as discussed in section 3.4 and considering good flowability, the best combination in this case is BFS4: FA 50:50 with 5% dosage of SF with a compressive strength of 46.4 N/mm2. It is also noted that

compressive strength of mortar increases with increasing fineness of BFS. For a given water-to-cement (w/c) ratio, an increase in specific surface area (cm2/g) generally results in an increased hydration rate and, therefore, improved early properties such as higher early strengths. (Dale P. Bentz, Edward J. Garboczi, Claus J. Haecker, & Ole M. Jensen, 1999). At a BFS4 blend ratio of 50% (BFS4: FA – 50:50), mix combination with BFS3 large mean particle size (low specific surface area) has the lowest strength at 38.7 N/mm^2 while that with BFS8 small mean particle size (high specific surface area) has the highest strength at 56.7 N/mm^2. It can be seen that at BFS: FA is 50:50, BFS8 SF (5%) has the highest strength than BFS3, BFS4 & BFS6.

5. Conclusions

It can be concluded from the studies that fresh properties and durability of high flow AAM concrete can be improved by optimizing the types, combination and blend ratio of powders from industrial by-products. It can also be concluded that self-compacting concrete with blast-furnace slag gives a good thermal cracking resistance and that drying shrinkage stress can be precisely analyzed by using the proposed reduction factor for Young's modulus. The main conclusions are summarized as follows.

(1) It was concluded that drying shrinkage stress can be precisely analyzed by adjusting the reduction factor for Young's modulus for the restraint stress analysis using 3-D FEM. And the new reduction coefficient for effective modulus of elasticity is proposed to precisely evaluate the influence of drying shrinkage on

(2) From FEM analysis of wall type structures, it is proved that partial replacement of blast furnace slag contributes to low temperature and improved cracking resistance at early age while drying shrinkage influences cracking resistance at an extended age.

(3) These approaches are therefore expected to increase usage of high flow concrete with industrial by-products as countermeasures to improve environmental conservation and sustainability.

(4) Yield value of AAM mortar decreases with an increase in BFS4 blend ratio but then dilatancy property increases when the BFS4 ratio increases up to 75% and more. For a BFS replacement ratio of 50%, silica fume dosage of 5% exhibits better flowability.

(5) Increasing blend ratio of BFS4 from 25% to 100% significantly increase 14-day compressive strength of AAM mortar subjected to steam curing. Increasing SF dosage from 0% to 10% is also able to slightly increase the compressive strength.

(6) Total pore volume of AAM paste decreases with increasing ratios of BFS4 and silica fume. In a similar manner, regardless of the mix proportion, compressive strength of AAM decreases as total pore volume increases. The volume of smaller pore diameter increases with the increasing BFS4 blend ratio.

(7) The new findings in this study are therefore expected to contribute to increasing the application of high flow concrete with industrial by-products as countermeasures to improve environmental conservation and sustainability.

References

1 Ouchi M., Nakamura, S., Osterberg, T., Hallberg, S-E and Lwin, Myint M. (2003), Applications of self-compacting concrete in Japan, Europe and the United States, International Seminar High Performance Concrete, Federal Highway Administration, USA

2 E. Rozière, S. Granger, Ph. Turcry and A. Loukili (2007), Influence of paste volume on shrinkage cracking and fracture properties of self-compacting concrete, Cement and Concrete Composites, vol. 29, no. 8, pp. 626-636.

3 Benson Kipkemboi and Shingo Miyazawa (2018), Properties and Thermal Stress Analysis of Blended Cement Self-Compacting Concrete, Open Journal of Civil Engineering, vol. 8, no. 2, pp. 102-120.

4 K. Nijs and M. Ishikawa (2017), Finite element implementation of a drying shrinkage model based on pore evaporation mechanics, in High Tech Concrete: Where Technology and Engineering Meet, Proceedings of the 2017 fib Symposium, Maastricht, Netherlands.

5 Japan Concrete Institute (2008), Guideline for Control of Cracking of Mass Concrete, Tokyo: Japan Concrete Institute.

6 Ryoichi A., Mizobuchi T. and Izumi H. (2019), Evaluation for apperent instantaneous stiffness decrease considering effect of creep of early age concrete, Cement Science and Concrete Technology, vol. 73, pp. 200-207.

7 Japan Society of Civil Engineers (2012), Standard Specifications for Concrete Structures.

8 Japan Society of Civil Engineers (2012), Recommendation for mix design and construction of self compacting concrete.

9 ASTM C 39 (2002), Standard test method for compressive strength of cylindrical concrete specimen, ASTM International.

10 Yasuyuki K., Hirotaka K. and Hiroshi W. (2002), A Study on estimation of adiabatic temperature rise charcteristics of high strength concrete by simple adiabatic test, Proceedings of the 57th Annual Conference of Japan Society of Civil Engineering, Japan.

11 Japan Concrete Institute (2017), Guideline for Control of Cracking of Mass Concrete 2016.

12 Japan Concrete Institute (1999), Autogenous Shrinkage of Concrete, 1st ed., E. Tazawa, Ed., E & FN SPON, London.
13 Benson Kipkemboi, Teng Zhao, Shingo Miyazawa, Etsuo Sakai, Nobukazu Nito and Hiroshi Hirao (2020), Effects of C_3S content of clinker on properties of fly ash cement concrete, Construction and Building Materials, vol. 240.
14 ASTM C157 / 157M (2008), Standard Test Method for Length Change of Hardened Hydraulic Cement Mortar and Concrete, ASTM International.
15 Y. Yang, R. Sato and K. Kawai (2001), Evaluation of autogenous shrinkage and drying shrinkage based on bound water content of cementitious materials, JSCE Preceedings.
16 American Concrete Institute (2013), ACI Concrete Terminology, in American Concrete Institute - Advancing concrete knowledge, Farmington Hills, Michigan.
17 J. M.Abdalhmid, A.F. Ashour and T. Sheehan (2019), Long-term drying shrinkage of self-compacting concrete: Experimental and analytical investigations, Construction and Building Materials, vol. 202, pp. 825-837.
18 Wang Guojie, Liu Jiding, Zheng Jianlan and Fan Wei (2018), Study on the stress relaxation properties of self-compacting concrete under restrained autogenous shrinkage, IOP Conf. Series: Materials Science and Engineering, vol. 431.
19 Shasha Xie, Zhiyuan Cheng and Li Wan (2019), Hydration and microstructure of astm type I cement paste, Sci Eng Com Materials, pp. 215-220.
20 Zhiwei Qu, Ruizhe Si, Pengjiao Jia and Yingda Zhang (2022), Creep and relaxation responses of fly ash concrete: Linear and nonlinear cases, Case Studies in Construction Materials, vol. 17.
21 Hiroshi Yamada, Hiroshi Katahira and Hiroshi Watanabe (2018), Estimation for drying shrinkage of concrete by composite model using coarse aggregate properties, Journal of Japan Society of Material Science, vol. 67, no. 3, pp. 396-400.
22 Kei-Ichi Imamoto (2008), Simplified prediction of drying shrinkage stress in reinforced concrete building wall, Advanced Concrete Technology - J-STAGE, vol. 6, no. 1, pp. 111-120.
23 Maruyama Ippei (2022), Impact of drying on concrete and concrete structures, RILEM Technical Letters.
24 Amir Hossein Ghorbankhani and Mahmoud Nili (2021), Experimental and numerical assessment of thermal properties of self-compacting mass concrete at early ages, European Journal of Environmental and Civil Engineering, vol. 26, no. 16, pp. 8194-8211.
25 C. Gallagher, E. Kerr and S. McFadden. (2023), Particle size distribution for additive manufacturing powder using stereological corrections. Powder Technology, 429. doi:10.1016/j.powtec.2023.118873

26 Dale P. Bentz, Edward J. Garboczi, Claus J. Haecker and Ole M. Jensen (1999), Effects of cement particle size distribution on performance properties of Portland cement-based materials. Cement and Concrete Research, 29(10), 1663 - 1671.

27 Etsuo Sakai, Keisuke Masuda, Yasuo Kakinuma and Yutaka Aikawa (2009), Effects of shape and packing density of powder particles on the fluidity of cement pastes with limestone powder. Journal of Advanced Concrete Technology, 7(3), 347 - 354.

28 Juntao Ma, Daguang Wang, Shunbo Zhao, Ping Duan and Shangtong Yang (2021), Influence of particle morphology of ground fly ash on the fluidity and strength of cement paste. Materials, 283(14).

29 Kong L., Fan Z., Ma W., Lu J. and Liu Y. (2021). Effect of curing conditions on the strength development of alkali-activated mortar. Crystals. doi:10.3390/cryst11121455

30 Maruoka M., Fujiwara H., Sugawara T., & Kawato T. (2016), Study on improvement of the properties of environment load - reduce high strength concrete. Cement Science and Concrete, 70, 328-335.

31 Provis L. John, & Jannie S.J Van Deventer (2014), Alkali Materials - State of the Art Report. RILEM - TC 224-AAM, 9-16.

32 Yamamoto Y., Homma A. and Kitsutaka Y. (1996). Study on the testing method of the rheological characteristics of high fluidity concrete, Journal of Structural & Construction Engineering, 9-16.

33 Yasser Rifaai, Ammar Yahia, Ahmed Mostafa, Salima Aggoun and El-Hadj Kadri (2019), Rheology and mechanical properties of alkali-activated hybrid matrix for self-consolidating concrete. Viktor Mechtcherine, Kamal Khayat, & Egor Secrieru (Eds.), Rheology and Processing of Construction Materials, 508-516, Springer.